Journal of Zhejiang University-SCIENCE A (Applied Physics & Engineering) *in press*
www.jzus.zju.edu.cn; www.springer.com/journal/11582
E-mail: jzus_a@zju.edu.cn

Research Article

https://doi.org/10.1631/jzus.A2500150

Continuous energy exchange between magnetic fields supporting memristive neuron firing

Zhao LEI[1], Qun GUO[1], Chunni WANG[2], Jun MA[1,2]✉

[1]*College of Electrical and Information Engineering, Lanzhou University of Technology, Lanzhou 730050, China*
[2]*Department of Physics, Lanzhou University of Technology, Lanzhou 730050, China*

Abstract: Biological neurons can be excited to maintain certain firing patterns following different external stimuli, and similar changes in electrical activities can be reproduced in some neural circuits by applying an external voltage. Generic neural circuits are composed of capacitors, induction coils, resistors, and nonlinear resistors, and continuous energy exchange between the capacitive and inductive components is crucial for preserving output voltages. Incorporating nonlinear elements causes interactions between the charge flow across the capacitor and the induced electromotive force on the inductor. It is a challenge to explore the occurrence of nonlinear oscillation and coherence resonance in a neural circuit without using a capacitor and nonlinear resistor, and it considers the case lack of electric field energy. In this paper, a simple neural circuit is proposed that combines two inductors, one magnetic flux-controlled memristor (MFCM), and three resistors, with two constant voltage sources in the branch circuits used as reverse potentials in the ion channels. The field energy has an exact form, and it is stored in the circuit components as a magnetic field. Scale transformation is applied on the circuit equations and field energy function to obtain equivalent dimensionless forms of the memristive neuron and Hamilton energy. The reference values for the physical time and capacitance are represented by an appropriate combination of resistance and inductance, because the capacitance value is unavailable. The memristive neuron without capacitive effect still shows similar firing patterns, and coherence resonance is induced under noisy excitation. The emergence of coherence resonance can be predicted by calculating the distribution of the average energy $\langle H \rangle$ versus noise intensity, and the value for $\langle H \rangle$ reaches a maximum under coherence resonance. Finally, an adaptive law for parameter growth under energy control is proposed to control mode transitions in the electrical activity. The methodology and results of this work offer insights into the oscillatory mechanism of neural circuits, and showcase how magnetic field control can be used to manage neural activations.

Key words: Neural circuit; Hamilton energy; memristor; stochastic resonance; adaptive parameter growth

1 Introduction

Changes in membrane potentials result in cascading electrical activities, with neurons maintaining suitable energy levels. These processes, which are facilitated by membrane ion channels, voltage-gate regulation, and local feedback loops, constitute neural circuits that serve as the fundamental units of neural information processing (Sporns, 2010) [1]. These circuits exhibit diverse firing patterns, such as spiking, bursting, and rhythmic firings; such firings can match with membrane responses, action potential timings, and postsynaptic integration effects (Douglas and Martin, 2004; Isaac et al, 1997) [2, 3]. Research has shown that neuronal firing is regulated not only by external stimuli, but also by the intrinsic energy level of a neuron and local synaptic inputs, especially inhibitory signals (Izhikevich, 2007; Wang, 2010; Buzsáki and Draguhn, 2004) [4–6]. For instance, Froemke et al. (Froemke et al, 2007) [7] found that inhibitory neurons can modulate the threshold for LTP (long-term potentiation) induction in excitatory neurons within specific circuits, thereby shaping the plasticity window. Moreover, Katz et al. (Katz and Shatz, 1996) [8] observed that spontaneous neuronal

✉ Jun MA, hyperchaos@lut.edu.cn
Zhao LEI, https://orcid.org/0000-0002-8046-0650
Chunni WANG, https://orcid.org/0000-0002-4688-7888
Jun MA, https://orcid.org/0000-0002-6127-000X

Received Apr. 25, 2025; Revision accepted June 2, 2025; Crosschecked

© Zhejiang University Press 2025

firing can form stable synaptic connectivity patterns, influencing a neuron's role within functional small-scale networks.

When neurons aggregate into localized functional regions, electromagnetic field coupling among cells can influence action potential propagation and synaptic plasticity, due to regulation of energy and controllable modification of ion channels (Takembo et al, 2019; Wang et al, 2019) [9, 10]. Takembo et al. (Takembo et al, 2019) [9] demonstrated that electromagnetic radiation alters the spatiotemporal patterns of membrane potentials within neural networks, affecting both synaptic coupling and plasticity. Wang et al. (Wang et al, 2019) [10] showed that electromagnetic induction and radiation via field coupling can modulate inter-neuronal communication, and that signal processing in a neural network can be activated under field coupling even when synaptic connections are removed. Neural networks maintain functional stability by regulating synaptic strength in order to balance excitation and inhibition; this balance is essential for their normal operation (Brütt and Christian, 2021; Chen et al, 2022; Kirischuk, 2022) [11–13]. Disruption of this balance may lead to pathological conditions such as epilepsy (Gao et al, 2017) [14]. Electromagnetic fields can regulate this balance by altering synaptic strengths, selectively enhancing or weakening specific connections in a parameter tuning approach (Dagar et al, 2016) [15]. Therefore, reconstructing neural circuits from the single-cell level not only reveals the fundamental principles of neural information encoding, but also provides cell-level intervention targets that aid understanding and treatment of neurological disorders (Altan et al, 2024) [16].

In traditional circuit theory, the dynamic exchange of energy is typically attributed to the interaction between electric field components (e.g., capacitors) and magnetic field components (e.g., inductors) (Schroedermeier and Ludois, 2016; Moon and Leeb, 2015; Li et al, 2016; Cheng et al, 2007) [17–20]. Capacitors serve as key energy storage elements, and provide the physical foundation for behaviors in oscillatory circuits such as periodic oscillation, signal modulation, and neuron-like firings (Indiveri et al, 2011) [21]. Consequently, most circuit designs rely heavily on capacitors to emulate the capacitive properties of neuron cell membranes (Jia et al, 2024; Yang and Ma, 2024; Wang et al, 2024; Wan et al, 2024; Yang et al, 2024; Jia et al, 2023) [22–27]. However, the relatively large physical dimensions and challenges of integrating capacitors hinder their application in high-density, flexible, and nanoscale neural networks. Thus, developing novel components and architectures without connecting capacitors, which can replicate neural circuit functionality and saving electric field energy, has become a critical focus in neuroelectronic engineering. However, lacking capacitors in a neural circuit presents new difficulties for scale transformation when the circuit equations are mapped to dimensionless theoretical models. This is because a reference capacitance is crucial for setting the reference time and energy. Therefore, an effective combination of electric components is crucial for realizing such scale transformations, and then nonlinear analysis can be calculated in the dimensionless models through a numerical approach.

Chua ever defined the concept of memristor in 1971, filling a role of the fourth basic circuit element after resistors, capacitors, and inductors. A memristor exhibits unique properties such as nonlinear modulation, memory retention, and dynamic energy responsiveness (Chua, 1971; Strukov et al, 2008; Pershin and Massimiliano, 2011) [28–30]. Based on their operational principles, memristors can be categorized into magnetic field-controlled memristors (MFCMs) and charge-controlled memristors (CCMs). MFCMs employ magnetic flux variation as the control variable, highlighting a bidirectional regulatory relationship between magnetic field flux and the memristive states (Li et al, 2021; Xu et al, 2024) [31, 32]. In contrast, CCMs are governed primarily by charge or voltage changes, offering faster response times and more mature device architectures. CCMs have been widely employed in large-scale memory arrays, artificial synaptic circuits, and low-power logic devices (Xu et al, 2024; Chen et al, 2015; Lei and Ma, 2025) [33–35]. Despite differences in their underlying mechanisms, both types of memristors play essential roles in the construction of neuromorphic circuits and functional enhancement of neural circuits.

The introduction of an MFCM into the branch circuit of a neural circuit supports energy shunting in

the form of magnetic flux. An MFCM-coupled neural circuit can estimate and describe the effect of a magnetic field, and its equivalent dimensionless model (a memristive neuron) often stores the magnetic flux variable; here, the memristive term is considered as an induction current for electromagnetic induction. Through combinations with a variety of sensing elements (such as thermistors, photocells, piezoelectric ceramics, and Josephson junctions), various functional neural circuits can be constructed. Such functional neurons can be sensitive to different external stimuli, such as temperature, light, mechanical vibrations, and magnetic fields (Ma et al, 2019; Ma, 2023) [36, 37].

In this study, two inductors connected in parallel are used to couple an MFCM, and external stimuli and noise radiation are applied to detect characteristic features of neural activity. An exact energy function for the neuron model is defined, and it is further proofed according to fundamental physical laws including the Helmholtz theorem. The average energy is analyzed statistically, and used to predict the stochastic resonance (SR), a phenomenon which is also observed in some mathematical and biological neuron models. In particular, during scale transformation from the circuit equations to the equivalent dimensionless neuron modes, [L/R] (=[T]) and [L/R^2] (=[C]) are employed as reference values to replace the time reference and capacitance reference, respectively. This scale transformation is effective for mapping the neural circuit to an effective neuron model, even though a capacitive variable is not used. Our methodology offers new theoretical insights and practical guidance for designing effective and robust neural circuits.

2 Model and scheme

The magnetic field components in this system primarily consist of inductors and an MFCM, which collectively serve as storage media for magnetic field energy. A major goal of this study is to verify whether this magnetic field-dependent circuit can generate spontaneous oscillations without utilizing capacitive field energy. When nonlinear activation and regulation from the MFCM are activated, the neural circuit in this work gains the capability to exhibit firing activities by pumping magnetic field among different ion channels/branch circuits of the neural circuit. In constructing equivalent oscillator-type theoretical models, the conversion of physical variables into dimensionless parameters using reference time and reference voltage is a critical modeling step. As illustrated in Fig. 1, we designed a minimalistic neural circuit architecture comprised of two inductors, one MFCM, and three resistors, which deliberately excludes conventional capacitive elements and nonlinear resistive components.

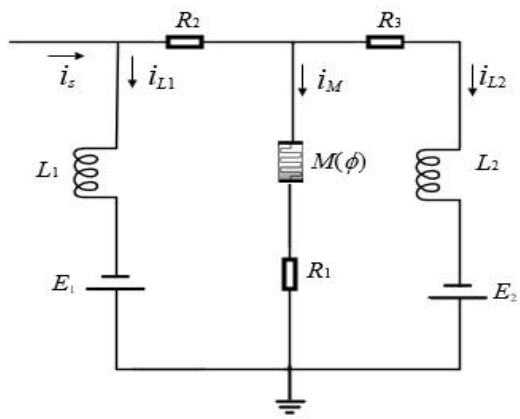

Fig. 1 The proposed MFCM coupled neural circuit driven by forcing current i_s. R_1, R_2, R_3, L_1, L_2, E_1, and E_2 denote resistors, inductors, and constant voltage sources, respectively.

Observing Fig. 1, the constant voltages E_1 and E_2 constrain the channel currents, and each can be considered as a reverse potential of ion channels in biological neurons. The linear resistors R_1, R_2, and R_3 balance the channel voltage through consumption of Joule heat. The branch circuit composed of the MFCM measures the membrane potential, and energy flow is shunted between the parallel branch circuits. The MFCM can be described by:

$$\begin{cases} i_M = M(\phi)V_M = \beta \csc(\phi) V_M, \\ i_M = i_S - i_{L1} - i_{L2}, \\ \dfrac{\mathrm{d}\phi}{\mathrm{d}t} = -K\phi + \delta V_M. \end{cases} \tag{1}$$

In Eq.(1), the parameter β accounts for the material properties of the MFCM, and the parameters (K, δ) estimate the effect of the magnetic field on the memristive channel /branch circuit. Indeed, the parameter $\delta = 1/N_0$ when the MFCM is considered as

an equivalent induction coil with N_0 turns, the parameter K estimates the effect of present magnetic field on the changes of magnetic flux and it holds physical unit as frequency. The field energy in the three components is estimated as follows:

$$\begin{cases} W_{L1} = \frac{1}{2} L_1 i_{L1}{}^2, \\ W_{L2} = \frac{1}{2} L_2 i_{L2}{}^2, \\ W_M = \frac{1}{2} \phi i_M, \\ W = \frac{1}{2} L_1 i_{L1}{}^2 + \frac{1}{2} L_2 i_{L2}{}^2 + \frac{1}{2} \phi i_M. \end{cases} \tag{2}$$

Equivalent conversion from physical variables to dimensionless variables is crucial for developing theoretical models from neural circuits. This is because the numerical solution approach should be independent of the physical units. The reference time [T], reference voltage [V_0], and reference capacitance [C] are important for the selection of reference values, and the symbol [*] signifies an operation on physical units. One of the constant voltages (E_1, E_2) can be used as a reference voltage V_0 for scale transformation on the physical variables, considering the elements in Fig. 1. Because of the absence of capacitor in the circuit in Fig. 1, an equivalent combination of other physical parameters is used to define equivalent reference values as follows (Guo and Ma, 2025) [38]:

$$\begin{aligned} [T] &= [\frac{Q}{I}] = [\frac{CV}{I}] = [RC] \\ &= [\frac{\Phi}{V}] = [\frac{LI}{IR}] = [\frac{L}{R}], \\ [C] &= [\frac{L}{R^2}]. \end{aligned} \tag{3}$$

where the operation [*] removes physical units from physical variables including voltage, current, charge, and time; T, R, C, L, Q, and I indicate physical time, resistance, capacitance, inductance, charge, and current intensity, respectively. The physical variables in Fig. 1 become coherent in following the circuit equations:

$$\begin{cases} L_1 \frac{\mathrm{d}i_{L1}}{\mathrm{d}t} = (i_s - i_{L1}) R_2 + V_M + i_M R_1 + E_1, \\ L_2 \frac{\mathrm{d}i_{L2}}{\mathrm{d}t} = V_M + i_M R_1 + E_2 - i_{L2} R_3, \\ \frac{\mathrm{d}\phi}{\mathrm{d}t} = -K\phi + \delta V_M. \end{cases} \tag{4}$$

There are three branch circuits in the neural circuit presented in Fig. 1, and no capacitive components are used. Neurons/cells have small geometric dimensions, and their capacitance values can be ignored when stochastic diffusion and intracellular ion pumping induce distinct magnetic fields. On the other hand, damage in capacitor or missing in capacitor requires new schemes for maintaining the electrical signals from the neural circuit. Therefore, two inductors and one MFCM are used in the three-branch circuits for describing the effect of the magnetic field and electromagnetic induction, respectively. When an external electric stimulus i_s is applied, energy is shunted between the three branches of the circuit and then the memristive channel is controlled to offer different memristive potentials accompanied by suitable energy levels. Following the definition for reference time in Eq. (3), some new variables and dimensionless gains are defined through:

$$\begin{cases} x = \frac{R_1 i_{L1}}{E_1}, y = \frac{R_1 i_{L2}}{E_1}, z = \frac{R_1 \phi}{L_1 E_1}, \tau = \frac{t R_1}{L_1}, \\ i_s' = \frac{i_s R_1}{E_1}, a = \frac{E_2}{E_1}, b = \frac{R_3}{R_1}, c = \frac{L_1}{L_2}, \\ r = \frac{R_2}{R_1}, k = K\frac{L_1}{R_1}, \sigma = \frac{L_1 E_1}{R_1}, \beta' = \frac{1}{\beta R_1}. \end{cases} \tag{5}$$

Inserting the new variables and parameters above into Eq. (4), and then a memristive oscillator is obtained by:

$$\begin{cases} \frac{\mathrm{d}x}{d\tau} = r i_s' - rx + (i_s' - x - y)(\beta' \sin(\sigma z) + 1) + 1, \\ \frac{\mathrm{d}y}{\mathrm{d}\tau} = c\left[(i_s' - x - y)(\beta' \sin(\sigma z) + 1) - by + a\right], \\ \frac{\mathrm{d}z}{\mathrm{d}\tau} = -kz + \delta(i_s' - x - y)\beta' \sin(\sigma z). \end{cases} \tag{6}$$

The external stimulus i'_s can be adjusted to modify the oscillatory state in the memristive neuron, even when all parameters are fixed. The voltage variable V_M can also be set to discern the firing modes as follows:

$$\begin{cases} V_M = \dfrac{i_S - i_{L1} - i_{L2}}{\beta \csc(\phi)}, \\ u = \dfrac{V_M}{E_1} = \left(i'_s - x - y\right)\beta' \sin\left(\sigma z\right). \end{cases} \tag{7}$$

As presented in Eq. (1), the mem-conductance has a csc(*) form, despite most previous research opting for a cubic or hyperbolic form. In fact, setting csc (*) mem-conductance or sin (*) mem-resistance for the memristor accounts for the polarization and depolarization of excitable media in a periodic fashion, because continuous electric excitations affect the neuron and excitable media. From a dynamic viewpoint, the memristor can be configured with different definitions for the relation between charge and magnetic flux, and then the memristive term with high-order nonlinearity can support continuous oscillation in the electrical activities. However, missing the capacitive variable as derived from a capacitor in the neural circuit prevents extensive energy exchange between the magnetic field and electric field. Therefore, carefully setting the memristive term for the neural circuit and its equivalent theoretical model requires periodic excitation to induce continuous electrical activities, and thus the csc(*) memristive term is useful. Consequently, the field energy in Eq. (2) is updated to a dimensionless form as follows:

$$\begin{cases} H_{L1} = \dfrac{1}{2}x^2, H_{L2} = \dfrac{1}{2c}y^2, \\ H_M = \dfrac{1}{2}z\left(i'_s - x - y\right), \\ H = \dfrac{R_1^2 W}{L_1 E_1^2} \\ \quad = \dfrac{1}{2}x^2 + \dfrac{1}{2c}y^2 + \dfrac{1}{2}z\left(i'_s - x - y\right). \end{cases} \tag{8}$$

That is, the Hamilton energy H converted from the field energy W has three terms, which are associated with the magnetic field in two inductors and the MFCM, respectively. Eq. (6) is rewritten in an equivalent vectorized form to approach its sole energy function following the Helmholtz theorem, in which the electromagnetic field is considered as a superposition of vortex field and gradient field:

$$\begin{aligned} \begin{pmatrix} \mathrm{d}x/\mathrm{d}\tau \\ \mathrm{d}y/\mathrm{d}\tau \\ \mathrm{d}z/\mathrm{d}\tau \end{pmatrix} &= \begin{bmatrix} ri'_s - rx + \left(i'_s - x - y\right)\left(\beta' \sin\left(\sigma z\right) + 1\right) + 1 \\ c\left[\left(i'_s - x - y\right)\left(\beta' \sin\left(\sigma z\right) + 1\right) - by + a\right] \\ -kz + \delta\left(i'_s - x - y\right)\beta' \sin\left(\sigma z\right) \end{bmatrix} \\ &= F_c(x,y,z) + F_d(x,y,z) \\ &= \nabla H^T J(x,y,z)\nabla H + \nabla H^T R(x,y,z)\nabla H \\ &= \begin{bmatrix} F_{cx} \\ F_{cy} \\ F_{cz} \end{bmatrix} + \begin{bmatrix} F_{dx} \\ F_{dy} \\ F_{dz} \end{bmatrix} \\ &= \begin{bmatrix} 0 & 0 & C_1 \\ 0 & 0 & C_2 \\ -C_1 & -C_2 & 0 \end{bmatrix} \begin{bmatrix} x - 0.5z \\ y/c - 0.5z \\ 0.5\left(i'_s - x - y\right) \end{bmatrix} \\ &\quad + \begin{bmatrix} A_1 & 0 & 0 \\ 0 & A_2 & 0 \\ 0 & 0 & A_3 \end{bmatrix} \begin{bmatrix} x - 0.5z \\ y/c - 0.5z \\ 0.5\left(i'_s - x - y\right) \end{bmatrix}, \end{aligned} \tag{9a}$$

$$\begin{aligned} C_1 &= 2 + 2\beta' \sin\left(\sigma z\right), \\ C_2 &= 2c + 2c\beta' \sin\left(\sigma z\right), \\ F_{cx} &= \left(i' - x - y\right)\left(\beta' \sin\left(\sigma z\right) + 1\right), \\ F_{cy} &= c\left[\left(i' - x - y\right)\left(\beta' \sin\left(\sigma z\right) + 1\right)\right], \\ F_{cz} &= \left(-2x - 2y + cz + z\right)\left(\beta' \sin\left(\sigma z\right) + 1\right), \\ F_{dx} &= ri'_s - rx + 1, F_{dy} = c\left[-by + a\right], \\ F_{dz} &= -kz + \delta\left(i'_s - x - y\right)\beta' \sin\left(\sigma z\right) \\ &\quad -\left(-2x - 2y + cz + z\right)\left(\beta' \sin\left(\sigma z\right) + 1\right), \\ A_1 &= \frac{ri'_s - rx + 1}{x - 0.5z}, A_2 = \frac{c\left[-by + a\right]}{y/c - 0.5z}, \\ A_3 &= \frac{F_{dz}}{0.5\left(i'_s - x - y\right)}. \end{aligned} \tag{9b}$$

Here, $F_c(x, y, z)$ and $F_d(x, y, z)$ represent the vortex field and gradient field, respectively. $J(x, y, z)$ is a skew-symmetric matrix, while $R(x, y, z)$ is a main diagonal matrix with elements including A_1, A_2, A_3. It is important to clarify why the decomposition in Eq. (9) still has physical significance, even though the field energy in Eq. (2) is only endowed with the

magnetic field form. In fact, two constant voltage sources are used in the circuit in Fig. 1, and they account for the resting potentials of the ion channels; however they also provide electric field energy. Therefore, decomposition of the theoretical model into vector form is meaningless when the neural circuit has no electric field component, and the dimensionless energy must be obtained by directly applying scale transformation to the physical field energy. Based on Helmholtz's theorem, the Hamilton energy function H for Eq. (8) meets the following criterion:

$$\begin{cases} \nabla H^T f_c(x,y,z) = 0, \\ \nabla H^T f_d(x,y,z) = \dot{H} = \dfrac{\mathrm{d}H}{\mathrm{d}\tau}. \end{cases} \tag{10}$$

Indeed, the energy function H in Eq. (8) satisfies the solution of Eq. (10) according to Eq. (9), and we simplify and validate this as follows:

$$\begin{aligned} \nabla H^T F_c &= F_{cx}\frac{\partial H}{\partial x} + F_{cy}\frac{\partial H}{\partial y} + F_{cz}\frac{\partial H}{\partial z} = 0, \\ \frac{\mathrm{d}H}{\mathrm{d}\tau} &= \left(x - \frac{1}{2}z\right)\frac{\mathrm{d}y}{\mathrm{d}\tau} + \left(\frac{y}{c} - \frac{1}{2}z\right)\frac{dy}{d\tau} \\ &\quad + \frac{1}{2}\left[i_s' - x - y\right]\frac{dz}{d\tau} \\ &= \left(x - \frac{1}{2}z\right)F_{dx} + \left(y - \frac{1}{2}cz\right)F_{dy} \\ &\quad + \frac{1}{2}\left(i_s' - x - y\right)F_{dz} \\ \nabla H^T F_d &= F_{dx}\frac{\partial H}{\partial x} + F_{dy}\frac{\partial H}{\partial y} + F_{dz}\frac{\partial H}{\partial z} = \frac{\mathrm{d}H}{\mathrm{d}\tau}. \end{aligned} \tag{11}$$

In fact, an exact solution of Eq. (10) is the same Hamilton energy function as presented in Eq. (8). Therefore, the Hamilton energy function for the memristive neuron can be obtained by applying scale transformation to the electric field energy components, and it can be proofed by applying the Helmholtz theorem. When the energy function is available, the average energy $\langle H \rangle$ provides a feasible way to predict the stochastic resonance and coherence resonance in the neuron under noisy excitation. For simplicity, Gaussian white noise with zero average value and intensity D can be used to excite the neuron from different branch circuits or ion channels. $\langle H \rangle$ represents the mean value of the energy function in Eq. (8) within a transient period, as the running time in the numerical approach.

Most biological neurons remain in a quiescent state until a powerful-enough external stimulus is applied to trigger firing patterns, because they are not self-oscillatory. In the absence of external stimuli, the neuron model has finite equilibrium points, while external periodic forcing will generate increasingly more, approaching infinite, equilibrium points. The appearance of unstable equilibrium points is crucial for inducing chaos in the oscillatory states and continuous firing patterns. According to Eq. (6), and following the constraints $\mathrm{d}x/\mathrm{d}\tau = \mathrm{d}y/\mathrm{d}\tau = \mathrm{d}z/\mathrm{d}\tau = 0$, the equilibrium points can be found according to the solution's dependence on the external excitation i'_s. At $i'_s = 0$, finite equilibrium points are obtained by solution with the following constraints:

$$\begin{cases} 0 = -rx - (x+y)\left(\beta'\sin(\sigma z) + 1\right) + 1, \\ 0 = -(x+y)\left(\beta'\sin(\sigma z) + 1\right) - by + a, \\ 0 = -kz - \delta(x+y)\beta'\sin(\sigma z). \end{cases} \tag{12}$$

On the other hand, $i'_s \neq 0$ enables infinite equilibrium points because it acts as a similar term to the jerk function sin (σz) in Eq. (6), and thus chaos and multiple firing patterns in the electrical activities occur. Assuming any constant value for i'_s, the corresponding Jacobi matrix and the dispersion relation are expressed by:

$$J = \begin{bmatrix} f_1 & f_2 & f_3 \\ g_1 & g_2 & g_3 \\ h_1 & h_2 & h_3 \end{bmatrix}. \tag{13}$$

The matrix elements and terms of Eq. (13) are given in Eq. (14), and a numerical solution can be obtained when all parameters are fixed:

$$\begin{cases} f_1 = -r - \beta' \sin(\sigma z) - 1, \\ f_2 = -\beta' \sin(\sigma z) - 1, \\ f_3 = i_s^{'} \beta' \sigma \cos(\sigma z) - \beta' \sigma (x + y) \cos(\sigma z), \\ g_1 = c\left[-\beta' \sin(\sigma z) - 1\right], \\ g_2 = c\left[-\beta' \sin(\sigma z) - 1 - b\right], \\ g_3 = c\left[i_s^{'} \beta' \sigma \cos(\sigma z) - \beta' \sigma (x + y) \cos(\sigma z)\right], \\ h_1 = -\delta\beta' \sin(\sigma z), h_2 = -\delta\beta' \sin(\sigma z), \\ h_3 = -k + \delta\beta' \sigma \left(i_s^{'} - x - y\right) \cos(\sigma z). \end{cases} \tag{14}$$

$$\begin{aligned} P(\lambda) = (\lambda - f_1)(\lambda - g_2)(\lambda + k) + \\ \delta f_3 g_1 + \delta f_2 g_3 - \delta f_3 g_2 - k f_2 g_1 - \delta f_1 g_3 . \end{aligned} \tag{15}$$

The system's numerical solutions become detectable when all parameters remain fixed. To examine noise effects, additive Gaussian white noise is independently introduced to affect each variable in Eq. (6), with each variable corresponding to an individual branch circuit in Fig. 1. Setting the parameters $a = 0.1$, $b = 7.2$, $c = 0.05$, $\delta = 1.5$, $\beta' = 3.2$, $k = 0.1$, $r = 0.1$, and $i'_s = 5.0$, fifteen eigenvalues are obtained and listed in the Table 1.

Table 1 Solutions and eigenvalues in Eq.(10)

/	Equilibrium points	λ_1	λ_2	λ_3
1	(5.944083652, -0.1118877271, -1.100935654)	79.66907219	-0.3438747826	-1.167342297
2	(6.075855048, -0.1100575688, 1.100744755)	92.66929547	-0.3438725449	-1.165224189
3	(6.066321320, -0.1101899817, 0.9414520500)	-0.3438743352	-1.166933581	-91.79956077
4	(5.953637127, -0.1117550399, -0.9413129975)	-0.3438724191	-1.165085770	-80.97805975
5	(6.038210594, -0.1105804084, 0.4717686726)	88.98267979	-0.3438730558	-1.165707400
6	(5.981737442, -0.1113647577, -0.4718035671)	83.41298105	-0.3438740018	-1.166602622
7	(6.019387128, -0.1108418454, 0.1572599350)	87.13175055	-0.3438733448	-1.165980873
8	(6.000562765, -0.1111032949, -0.1572638084)	85.27530538	-0.3438736594	-1.166278452
9	(6.057033217, -0.1103189831, 0.7862633296)	90.82842603	-0.3438727898	-1.165455828
10	(5.962911096, -0.1116262348, -0.7863604453)	81.54438138	-0.3438743751	-1.166956181
11	(6.047538405, -0.1104508555, 0.6276208446)	-0.3438740793	-1.166686571	-90.00420332
12	(5.972415410, -0.1114942304, -0.6275591899)	-0.3438728107	-1.165463072	-82.79059229
13	(6.028756301, -0.1107117180, 0.3138032030)	-0.3438738013	-1.166418244	-88.20582606
14	(5.991194744, -0.1112334063, -0.3137878112)	-0.3438731696	-1.165808991	-84.59923658
15	(6.009975062, -0.1109725686, 0.)	-0.3438734988	-1.166126501	-86.40423937

By systematically adjusting the noise intensity, we can observe its dynamic influence on both the shift in energy levels and the electrical activity patterns. This modulation approach enables effective detection of subtle system state changes. Our investigation reveals that when external energy is injected into the memristive channel, it is redistributed to the two parallel inductive channels. This unique energy reallocation mechanism not only sustains continuous oscillations in the neural circuit, but also ensures stable electrical activities in the memristive neuron.

3 Numerical results and discussion

The time series values of the three variables in Eq.(6) and the memristive potential u in Eq.(7) are calculated by using the fourth-order Runge-Kutta algorithm. The external stimulus is selected as a sinusoidal excitation $i'_s = A \sin(\omega\tau)$, where A is the amplitude and ω is the frequency. In Fig. 2, we conducted an equilibrium point analysis and dynamical characterization by measuring the peak values, and the largest Lyapunov exponent (LLE) is estimated from the sampled time series for one variable.

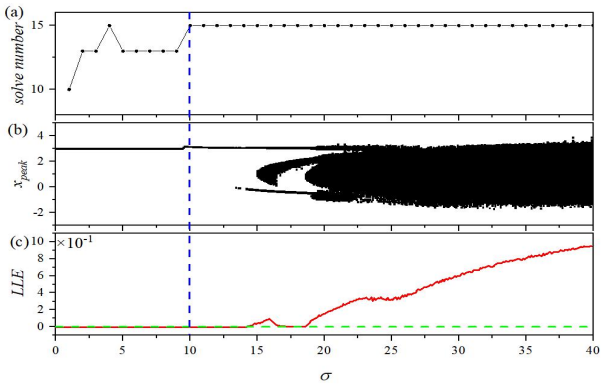

Fig. 2 (a) Number of equilibrium points at i'_s = 5; (b) Peak value in sampled time series for variable x; (c) LLE vs. parameter σ. For (b,c) $i'_s = 5\sin(\omega\tau) = 5\sin(2.5\tau)$. Parameters are set to: $a = 0.1$, $b = 7.2$, $c = 0.05$, $\delta = 1.5$, $\beta' = 3.2$, $r = 0.1$, $k = 0.1$, with initial values (2.0, 2.0, 0.01).

The parameter σ governs the transition pathway of the system from low-dimensional stable states with simple structures, to high-dimensional complex dynamical behaviors. As σ increases beyond a critical threshold, the emergence of positive LLE values and the proliferation of equilibrium points collectively demonstrate characteristic bifurcation patterns, marking the system's evolution from stability to chaos. To further investigate this transition, we examined the system's response under a different driving frequency (ω = 10) while holding the other parameters consistent with the configuration in Fig. 2. The bifurcation diagram is presented in Fig. 3.

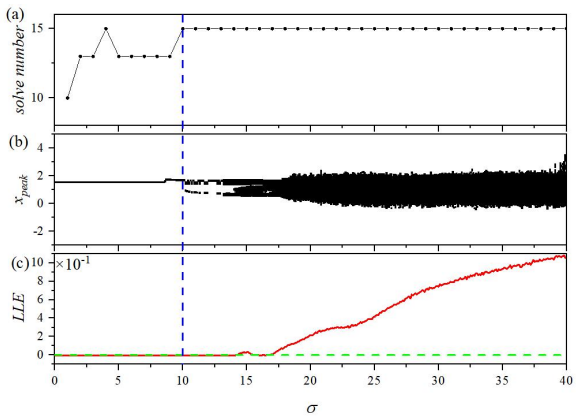

Fig. 3 (a) Number of equilibrium points at i'_s = 5; (b) Peak value in sampled time series for variable x; (c) LLE vs. parameter σ. For (b,c) $i'_s = 5\sin(\omega\tau) = 5\sin(10\tau)$.

The system exhibits a pronounced transition at $\sigma \approx 10$, which is a critical threshold that demarcates the shift from low-dimensional steady states to multi-stability and chaotic regimes. This transition demonstrates that σ in the memristive function is the principal parameter controlling structural reconfiguration. Our investigations reveal that increasing the external excitation frequency promotes the proliferation of equilibrium points, and facilitates the emergence of chaotic behavior within identical σ parameter ranges. The parameter σ predominantly governs the system's nonlinear activation intensity, while the external excitation frequency modulates the dynamic characteristics and information complexity. Systematic bifurcation analysis is conducted through adjustment of the forcing frequency ω, with the corresponding results presented in Fig. 4.

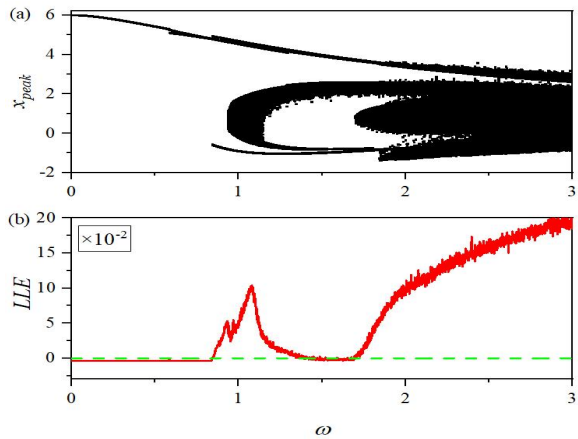

Fig. 4 Distribution of peak values and LLE vs. angular frequency ω. The parameters were set to: $a = 0.1$, $b = 7.2$, $c = 0.05$, $\delta = 1.5$, $\sigma = 20.0$, $\beta' = 3.2$, $k = 0.1$, $A = 5$, and $r = 0.1$.

The results demonstrate that the memristive neuron exhibits chaotic patterns when the forcing frequency ω ranges from 0.85 to 1.4 or exceeds 1.7, with higher forcing frequencies being more likely to support chaotic activity. The results in Fig. 4 help identify parameter ranges that can distinguish chaotic and periodic attractors. Furthermore, Fig. 5 illustrates the evolution of attractors and the variable x under varying external stimuli frequencies, providing insights into how firing patterns depend on the excitation frequency.

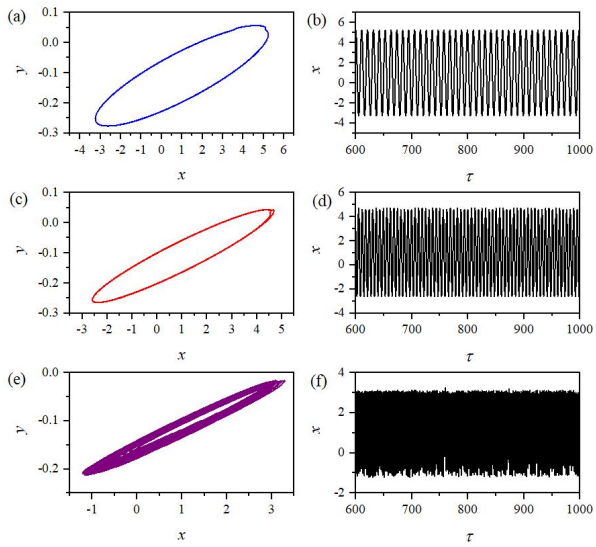

Fig. 5 (a, c, e) System attractor; (b, d, f) Evolution of the variable *x*. For (a, b) ω = 0.6; (c, d) ω = 1.0; (e, f) ω = 2.5.

Under external excitation currents with varying frequencies, the memristive neuron exhibits multiple oscillation modes, including periodic, weakly chaotic, and strongly chaotic states. Specifically, periodic attractors correspond to regular spiking patterns; weakly chaotic attractors maintain overall periodicity while displaying localized chaos in the upper-right region; strongly chaotic attractors display a complete loss of periodicity and have fully irregular dynamics. Analysis of the energy reveals that chaotic neurons maintain lower average energy values <*H*> compared to periodic neurons, suggesting that energy relationships dominate the mode transitions. Fig. 6 presents a quantitative comparison of energy variations and the proportion of energy components across different regimes.

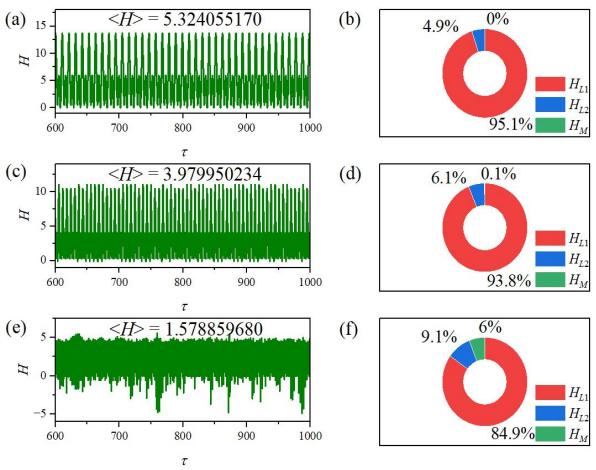

Fig. 6 (a, c, e) Evolution of the energy function; (b, d, f) Energy proportion for each energy term in the neuron presenting with different firing patterns. For (a, b) ω = 0.6; (c, d) ω = 1.0; (e, f) ω = 2.5.

Fig. 6 demonstrates that the average energy in the strongly chaotic state is markedly lower than in the periodic and weakly chaotic states. The emergence of chaotic behavior shows a direct correlation with the relative proportion of memristive channel energy *M*, where increasing *M* and L_2 proportions lead to greater chaos in the system. Using the parameter configurations from Figs. 5 and 6, we calculated the voltage variables in the memristive channel to identify the distinct firing patterns, which are displayed in Fig. 7.

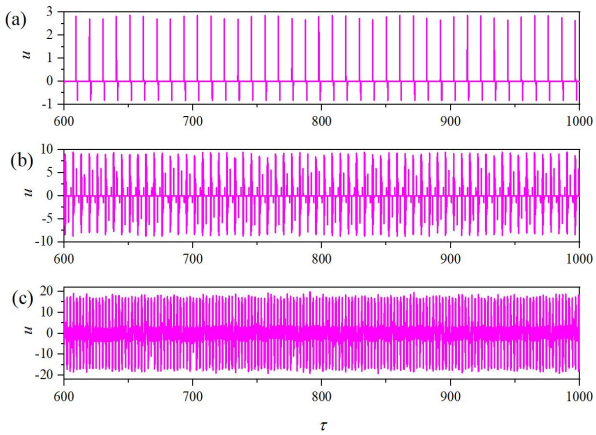

Fig. 7 Evolution of the memristive variable *u* in Eq. (6). For (a) ω = 0.6; (b) ω = 1.0; (c) ω = 2.5.

When varying the forcing frequency ω to evoke periodic or chaotic electrical activities in neurons, the firing patterns in Fig. 7 exhibit significant frequency-dependent variations, particularly demonstrating strongly chaotic firings. Furthermore, we added Gaussian white noise to the single-variable/branch circuit, and employed both the coefficient variation (*CV*) and average energy <*H*> as quantitative metrics to detect the occurrence of stochastic resonance:

$$\begin{cases} CV = \dfrac{\sqrt{\langle ISI^2 \rangle - \langle ISI \rangle^2}}{\langle ISI \rangle}, \\ \langle H \rangle = \dfrac{1}{t_1 - t_0} \displaystyle\int_{t_0}^{t_1} H d\tau = \dfrac{1}{N} \sum_{i=1}^{N} H_i. \end{cases} \tag{16}$$

Here, the *ISI* (inter-spike interval) can be obtained from the sampled variable series for one variable in the model. *N* describes the maximum count or number of iterations in the numerical calculation. In Fig. 8, the dependence of *CV* values and average energy <*H*> on the noise intensity is estimated to predict the emergence of stochastic resonance; this results in the maximum value for <*H*> and the lowest value for *CV* occurring at a moderate noise intensity.

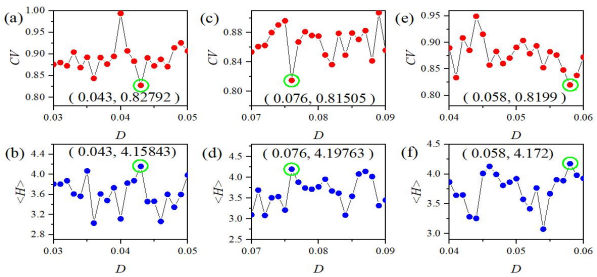

Fig. 8 Distribution of *CV* values and <*H*> versus noise intensity *D* at *ω* = 1.0, for (a, b) noise excitation on the variable *x*; (c, d) noise excitation on the variable *y*; (e, f) noise excitation on the variable *z*.

In Fig. 8, the numerical simulations demonstrate characteristic stochastic resonance (SR) phenomena when the noise intensity reaches appropriate levels, manifesting as highly synchronized neural activity and consistent correspondence between the minimum value for *CV* and maximum value for <*H*>. Quantitative analysis reveals that: SR occurs in the L_1 inductive channel (D = 0.043) with <*H*> = 4.15843 and CV = 0.82792; the L_2 inductive channel (D = 0.076) exhibits an enhanced SR response (<*H*> = 4.19763, CV = 0.81505); and the memristive channel shows SR at D = 0.058 (<*H*> = 4.172, CV = 0.8199). A comparative analysis indicates that the L_2 channel achieves optimal SR performance under noise excitation, demonstrating both the highest <*H*> value and lowest *CV* value, which suggests its superior responsiveness to noise modulation. Furthermore, Fig. 9 presents a comparison of the response characteristics of the neuron when three branch circuits are simultaneously excited by identical noise excitations.

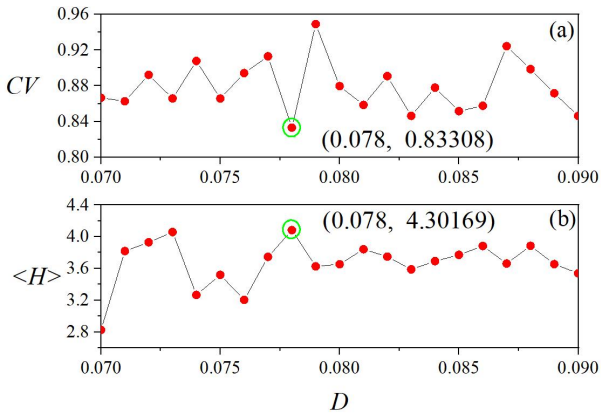

Fig. 9 Distribution of *CV* values and <*H*> vs. noise intensity *D* at *ω* = 1.0.

It is worth noting that when the three variables in Eq. (6) are simultaneously excited by the same noise, the system also exhibits SR at moderate noise intensity. In the unique configuration of a purely magnetic circuit, the energy exchange among the three channels/branches becomes much more intricate. Compared to the single-channel stimulation case illustrated in Fig. 8, the enhanced inter-channel coupling notably raises the noise intensity threshold required to achieve SR. Moreover, under multi-channel excitation, the maximum value of <*H*> exceeds the value that was observed under single-channel noise, while the *CV* value falls below the minimum *CV* recorded in the single-channel scenario. These findings indicate that synergistic interactions among multiple channels contribute to a more effective activation of SR, highlighting the advantages of multi-branch magnetic structures in enhancing neural circuit functionality. To further investigate adaptive regulation based on the mode selection in neural activities, an adaptive control scheme for the parameter *σ* following the energy regulation is suggested as follows:

$$\begin{cases} \dfrac{d\sigma}{d\tau} = -g\sigma \cdot \theta\left(\left|\dfrac{H_M(\tau)}{H(\tau)}\right| - \varepsilon\right), \\ \theta(v) = 1, v \geq 0, \theta(v) = 0, v < 0, \tau > 650. \end{cases} \tag{17}$$

In this control scheme, the proportional threshold *ε* determines the ratio of memristive channel energy to the total electric field energy of the neuron, the parameter *g* controls the growth rate of the gain *σ* for memristive current, and *θ* represents the

Heaviside function. Adaptive control is activated at $\tau > 650$ so that the neuron is activated during the transition period, showing a stable firing pattern.

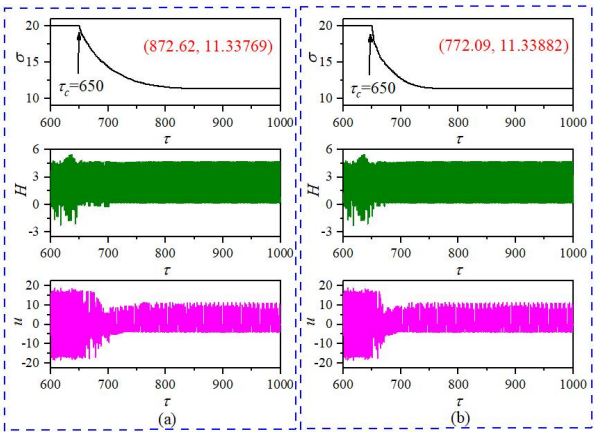

Fig. 10 The change of parameter σ in Eq. (6) with the evolution of Hamilton energy H and memristive variable u. For (a) $g = 0.03$; (b) $g = 0.05$. The parameters are set to: $a = 0.1$, $b = 7.2$, $c = 0.05$, $\beta' = 3.2$, $k = 0.1$, $A = 5.0$, $\omega = 2.5$, $r = 0.1$, and $\varepsilon = 0.3$.

As shown in Fig. 10(a), when the parameter g = 0.03, the control parameter σ stabilizes at 11.33769 after 872.62 (= 650 + 222.62) time units. Under adaptive control, the neural activities show distinct transitions from chaotic to periodic states, which are accompanied by significant changes in the energy function. The results in Fig. 10 confirm that increasing the parameter g will significantly reduce the time before the parameter σ attains a saturation value, thereby accelerating the transition from chaotic to periodic states. The memristive variable u of the memristor also changes to a periodic oscillation.

In summary, activation of energy flow across the magnetic field is effective for supporting continuous changes in the neural circuit composed of inductive components and MFCM. Moreover, this memristive neuron without a capacitive variable still presents similar firing patterns as known neuron models. Our proposed neuron generates diverse firing patterns, which can be characterized by measuring the voltage across the MFCM in the neural circuit. Its oscillatory mechanism results from continuous energy exchange between the memristive channel and inductive channels. The numerical results confirm that continuous energy exchange serves as the physical foundation for sustaining neuronal oscillations and stable firing patterns. Notably, the high-order nonlinearity of the memristor governs the emergence of chaotic behavior by determining the number of equilibrium points. Precise adjustment of the external stimulation frequency ω enables controlled transitions between firing patterns and effective energy level modulation, while significant SR is induced under appropriate noise intensity. This novel pure magnetic-field circuit architecture may aid both neurodynamic research and neuromorphic device design. In recent decades, memristors with varying memristive functions have been used to design and control nonlinear circuits. The initial dependence and memory properties enable multi-stability and applications in neural circuits; as such, functional neurons with clear physical descriptions have been developed (Shao et al, 2024; Wu and Wang, 2023; Babacan et al,2016; Ascoli and Corinto, 2013; Shi et al, 2024) [39-43]. In particular, this approach offers an exact energy definition for the memristive oscillator, and the memristive map provides physical explanations for the memristive systems (Li and Chen, 2023; Mao et al, 2025; Shi et al, 2024; Du et al, 2022) [44-47]. Moreover, the energy balance supports synchronization and regularized patterns in coupled biophysical models. And with reliable neuron models, energy control can be helpful for preventing nervous disorders (Hou et al, 2024; Zhao et al, 2024) [48, 49]. At the same time, the proposed neuron models can be further updated with equivalent map neurons (Guo et al, 2024; Jia et al, 2024) [50, 51] by applying linear transformations or the Euler difference algorithm. Additionally, digital implementation of neuron models via an FPGA (Field Programmable Gate Array) (Graas et al, 2004; Wang and Luo, 2022; Liu et al, 2024) [52-54] enables rapid parallel computing of neural signals in coupled circuit arrays, which can be used to improve control of electromechanical devices through maintenance of neural signals.

4 Conclusions

An MFCM was incorporated into a branch circuit of a capacitor-free linear circuit, transforming the circuit into a pure magnetic-field system; this memristive term/channel played an important role in shunting energy and regulating nonlinear energy without using any capacitive variables. Conventional theory holds that oscillatory circuits and their

equivalent nonlinear oscillators arise from energy exchange between storage elements for electric fields and magnetic fields, and that pure magnetic-field circuits are generally incapable of such energy interactions. However, in this study we successfully demonstrated energy exchange in a pure magnetic-field circuit through a novel MFCM-based neural circuit, and it was confirmed that the energy proportion in the magnetic channel significantly influences the system's firing modes. Moreover, simulation results showed that under different external stimulation frequencies, the MFCM acts as a temporary energy storage unit, inducing various firing patterns by activating electromagnetic induction in the memristive channel.

Our proposed scheme demonstrates that the combination of an inductor and an MFCM can establish a functional neural circuit that does not require capacitors. In the developed memristive model, the energy function exhibits unique determinacy. The capacitor-free design not only eliminates geometric constraints associated with capacitors, but also enables the memristor terminal voltage to be directly equated to neuron membrane potential. The findings further showcase that efficient neural circuit implementation can be achieved through proper configuration of non-capacitive electrical elements, such as inductors, resistors, and MFCMs. This work advances beyond the conventional limitation that pure magnetic-field circuits cannot achieve continuous energy exchange, and provides a theoretical foundation for developing novel capacitor-free neural circuits where even nonlinear resistors may not be used. This novel incorporation of an MFCM expands memristor applications in nonlinear circuits, and potentially opens technical pathways for biomimetic neuromorphic computing systems in the future. Subsequent research will focus on optimizing the dynamic characteristics of incorporated MFCMs, as well as the performance and adaptability of memristive models in computational neuroscience.

Acknowledgments

This work is supported by the National Natural Science Foundation of China (No. 62361037).

Author contributions

Jun MA and Zhao LEI designed the research. Zhao LEI and Qun GUO processed the corresponding data. Zhao LEI wrote the first draft of the manuscript. Chunni WANG supports funding for this research. Jun MA and Chunni WANG revised and edited the final version.

Conflict of interest

Zhao LEI, Qun GUO, Chunni WANG and Jun MA declare that they have no conflict of interest.

References

[1] Sporns O. Networks of the Brain. Cambridge: MIT Press 2010. doi: 10.7551/mitpress/8476.001.0001.

[2] Douglas RJ, Martin KAC. Neuronal circuits of the neocortex. Annual Review of Neuroscience 2004, 27: 419-451.

[3] Isaac JTR, Crair MC, Nicoll RA, et al. Silent synapses during development of thalamocortical inputs. Neuron 1997, 18: 269-280.

[4] Izhikevich EM. Dynamical Systems in Neuroscience: The Geometry of Excitability and Bursting. MIT Press, 2007.

[5] Wang XJ. Neurophysiological and computational principles of cortical rhythms in cognition. Physiological Reviews 2010, 90: 1195-1268.

[6] Buzsáki G, Draguhn A. Neuronal oscillations in cortical networks. Science 2004, 304(5679): 1926-1929.

[7] Froemke RC, Merzenich MM, Schreiner CE. A synaptic memory trace for cortical receptive field plasticity. Nature 2007, 450(7168): 425-429.

[8] Katz LC, Shatz CJ. Synaptic activity and the construction of cortical circuits. Science 1996, 274(5290): 1133-1138.

[9] Takembo CN, Mvogo A, Ekobena Fouda HP, et al. Effect of electromagnetic radiation on the dynamics of spatiotemporal patterns in memristor-based neuronal network. Nonlinear Dynamics 2019, 95:1067- 1078.

[10] Wang C, Tang J, Ma J. Minireview on signal exchange between nonlinear circuits and neurons via field coupling. European Physical Journal Special Topics 2019, 228: 1907-1924.

[11] Brütt M, and Christian K. On the role of the excitation/inhibition balance of homeostatic artificial neural networks. Entropy 2021, 23.12: 1681.

[12] Chen L, Li X, Tjia M, et al. Homeostatic plasticity and excitation-inhibition balance: The good, the bad, and the ugly. Current Opinion in Neurobiology 2022, 75: 102553.

[13] Kirischuk S. Keeping excitation–inhibition ratio in balance. International Journal of Molecular Sciences 2022, 23.10: 5746.

[14] Gao R, Peterson EJ, Voytek B. Inferring synaptic excitation/inhibition balance from field potentials. Neuroimage 2017, 158, 70-78.

[15] Dagar S, Chowdhury SR, Bapi RS, et al. Near-infrared spectroscopy-electroencephalography-based brain-state-dependent electrotherapy: a computational approach based on excitation-inhibition balance hypothesis. Frontiers in Neurology 2016, 7: 123.

[16] Altan MA, Orman K, Babacan Y, et al. Special memristor

and memristor-based compact neuron circuit. Journal of Circuits, Systems and Computers 2024, 33:2450091.
[17] Schroedermeier A, Ludois DC. Integrated inductor and capacitor with co-located electric and magnetic fields. IEEE Transactions on Industry Applications 2016, 53: 380-390.
[18] Moon J, Leeb SB. Power electronic circuits for magnetic energy harvesters. IEEE Transactions on Power Electronics 2015, 31: 270-279.
[19] Li S, Liu Z, Zhao H, et al. Wireless power transfer by electric field resonance and its application in dynamic charging. IEEE Transactions on Industrial Electronics 2016, 63: 6602-6612.
[20] Cheng S, Wang N, Arnold DP. Modeling of magnetic vibrational energy harvesters using equivalent circuit representations. Journal of Micromechanics and Microengineering 2007, 17: 2328.
[21] Indiveri G, Linares-Barranco B, Hamilton T J, et al. Neuromorphic silicon neuron circuits. Frontiers in Neuroscience 2011, 5:73.
[22] Jia J, Xie Y, Wang C, et al. Thermosensitive double-membrane neurons and their network dynamics. Physica Scripta 2024, 99: 115030.
[23] Yang F, Ma J, Wu F. Review on memristor application in neural circuit and network. Chaos, Solitons & Fractals 2024, 187: 115361.
[24] Wang B, Lv M, Zhang X, et al. Dynamics in a light-sensitive neuron with two capacitive variables. Physica Scripta 2024, 99: 055225.
[25] Wan J, Wu F, Ma J, et al. Dynamics and synchronization of neural models with memristive membranes under energy coupling. Chinese Physics B 2024, 33: 050504.
[26] Yang F, Ma J, Ren G. A Josephson junction-coupled neuron with double capacitive membranes. Journal of Theoretical Biology 2024, 578: 111686.
[27] Jia J, Yang F, and Ma J. A bimembrane neuron for computational neuroscience. Chaos, Solitons & Fractals 2023, 173: 113689.
[28] Chua LO. Memristor-The missing circuit element. IEEE Transactions on Circuit Theory 1971, 18: 507-519.
[29] Strukov DB, Snider GS, Stewart DR, et al. The missing memristor found. Nature 2008, 453(7191): 80-83.
[30] Pershin YV, Massimiliano DV. Memory effects in complex materials and nanoscale systems. Advances in Physics 2011, 60: 145-227.
[31] Li C, Yang Y, Du J, et al. A simple chaotic circuit with magnetic flux-controlled memristor. The European Physical Journal Special Topics 2021, 230: 1723-1736.
[32] Xu Q, Fang Y, Feng C, et al. Firing activity in an N-type locally active memristor-based Hodgkin-Huxley circuit. Nonlinear Dynamics 2024, 112:13451-64.
[33] Xu Q, Ding X, Wang N, et al. Spiking activity in a memcapacitive and memristive emulator-based bionic circuit. Chaos, Solitons & Fractals 2024, 187:115339.
[34] Chen ZQ, Tang H, Wang ZL, et al. Design and circuit implementation for a novel charge-controlled chaotic memristor system. Journal of Applied Analysis and Computation 2015, 5: 251-261.
[35] Lei Z, and Ma J. Coherence resonance and energy dynamics in a memristive map neuron. Chaos: An Interdisciplinary Journal of Nonlinear Science 2025, 35:023158.
[36] Ma J, Yang ZQ, Yang LJ, Tang J. A physical view of computational neurodynamics. Journal of Zhejiang University-Science A 2019, 20:639-59.
[37] Ma J. Biophysical neurons, energy, and synapse controllability: a review. Journal of Zhejiang University-Science A 2023, 24:109-29.
[38] Guo YT, Ma J. An electromechanical arm model controlled by artificial muscles. Science China Technological Science 2025, 68:1420403.
[39] Shao Y, Wu F, Wang Q. Synchronization and complex dynamics in locally active threshold memristive neurons with chemical synapses. Nonlinear Dynamics 2024, 112:13483-502.
[40] Wu F, Wang R. Synchronization in memristive HR neurons with hidden coexisting firing and lower energy under electrical and magnetic coupling. Communications in Nonlinear Science and Numerical Simulation 2023, 126:107459.
[41] Babacan Y, Kaçar F, Gürkan K. A spiking and bursting neuron circuit based on memristor. Neurocomputing 2016, 203:86-91.
[42] Ascoli A, Corinto F. Memristor models in a chaotic neural circuit. International Journal of Bifurcation and Chaos 2013, 23:1350052.
[43] Shi S, Liang Y, Li Y, et al. A neuron circuit based on memristor and negative capacitor: Dynamics analysis and hardware implementation. Chaos, Solitons & Fractals 2024, 180:114534.
[44] Li Z, Chen K. Neuromorphic behaviors in a neuron circuit based on current-controlled Chua Corsage Memristor. Chaos, Solitons & Fractals 2023, 175:114017.
[45] Mao Y, Dong Y, Lu Z, et al. Second-order locally active memristor based neuronal circuit. Chaos, Solitons & Fractals 2025, 195:116279.
[46] Shi F, Cao Y, Banerjee S, et al. A neuronal circuit based on a second-order memristor. Nonlinear Dynamics 2024, 113: 12165-12183.
[47] Du S, Deng Q, Hong Q, et al. A memristor-based circuit design and implementation for blocking on Pavlov associative memory. Neural Computing and Applications 2022, 34:14745-61.
[48] Hou S, Wang H, Fan D, et al. The Effects of Negative Regulation on the Dynamical Transition in Epileptic Network. International Journal of Bifurcation and Chaos 2024, 34:2450038.
[49] Zhao J, Yu Y, Han F, et al. Dynamic modeling and closed-loop modulation for absence seizures caused by abnormal glutamate uptake from astrocytes. Nonlinear Dynamics 2024, 112:3903-3916.
[50] Guo Y, Ma J, Zhang X, Hu X. Memristive oscillator to

memristive map, energy characteristic. Science China Technological Sciences 2024, 67:1567-1578.
[51] Jia J, Wang C, Zhang X, Zhu Z. Energy and self-adaption in a memristive map neuron. Chaos, Solitons & Fractals 2024, 182:114738.
[52] Graas EL, Brown EA, Lee RH. An FPGA-based approach to high-speed simulation of conductance-based neuron models. Neuroinformatics 2004, 2:417-4135.
[53] Wang C, Luo Z. A review of the optimal design of neural networks based on FPGA. Applied Sciences 2022, 12:10771.
[54] Liu F, Li H, Hu W, et al. Review of neural network model acceleration techniques based on FPGA platforms. Neurocomputing 2024, 610:128511.

中文概要

题　目：持续的磁场能量交换维系忆阻神经元的放电

作　者：雷召[1]，郭群[1]，王春妮[2]，马军[1,2]
机　构：[1]兰州理工大学，电气工程与信息工程学院，中国兰州，730050；[2]兰州理工大学，理学院，中国兰州，730050；

目　的：神经元电路的振荡源于其内部电场和磁场能量的持续交换。当电容器损坏或者缺失时，对神经元电路进行改造并产生连续的神经电信号非常关键。神经元电路通常包含电容器，电感线圈、电阻和非线性器件，这些非线性电路的动力学分析必须在无量纲模型中进行。在对电路方程进行标度变化时需要引入时间标度和电压标度，时间标度一般包含RC，当电容器缺失时则时间标度则无法直接定义。因此，定义新的时间标度就具有重要的科学意义。

创新点：1. 在电容参量C缺失时以电感参数和电阻参数的组合定义了新的时间基准和能量基准(标度变换的基准值)。2. 神经元电路能量以磁场方式存储于磁控忆阻器和感应线圈支路，持续的能量交换保障了神经元电路持续振荡。3. 定义了场能量函数和对应的哈密顿能量函数，解释了放电模态对能量的依赖性，进一步提出基于能量控制的自适应律来控制参数增长。

方　法：1. 采用单个磁控忆阻器并联两个电感线圈，在线圈支路引入恒定电压源表示离子通道反转电位。2. 计算了神经元各个支路场能量，并利用标度变换把神经元电路场能量函数转化为无量纲的形式，该能量函数进一步利用赫姆霍兹定理得以证明。3. 计算该忆阻神经元模型的变量序列进行分岔分析，进一步施加通道噪声诱发随机共振并利用哈密顿能量函数平均值来预测随机共振。4. 基于能量流对神经元参数进行自适应调控，以实现对放电模态的控制。

结　论：1. 神经元电路的持续振荡源于各个支路器件持续的能量交换。2. 电容器缺失时基于磁控的元件如电感线圈和磁控忆阻器，在支路恒定电压源驱动下神经元电路依然能产生持续电信号。3. 能量值决定着神经元的放电模态，能量操控可以改变神经元的放电特征。4. 没有时变电场的神经元电路和无电容性变量的忆阻神经元同样有效展示神经元电活动的动力学特征。

关键词：神经元电路；哈密顿能量；忆阻器；随机共振；自适应参数增长